American Mineralogist, Volume 87, pages 1546–1556, 2002

Characterization and modeling of illite crystal particles and growth mechanisms in a zoned hydrothermal deposit, Lake City, Colorado

D.J. BOVE,[1,*] D.D. EBERL,[2] D.K. MCCARTY,[3] AND G.P. MEEKER[1]

[1]U.S. Geological Survey, P.O. Box 25046, MS 905, Denver, Colorado 80225, U.S.A.
[2]U.S. Geological Survey, 3215 Marine Street, Suite E-127, Boulder, Colorado 80303-1066, U.S.A.
[3]Texaco EPTD, 3901 BriarPark, Houston, Texas 77042, U.S.A.

ABSTRACT

Mean thickness measurements and crystal-thickness distributions (CTDs) of illite particles vary systematically with changes in hydrothermal alteration type, fracture density, and attendant mineralization in a large acid-sulfate/Mo-porphyry hydrothermal system at Red Mountain, near Lake City, Colorado. The hydrothermal illites characterize an extensive zone of quartz-sericite-pyrite alteration beneath two deeply rooted bodies of magmatic-related, quartz-alunite altered rock.

Nineteen illites from a 3000 ft vertical drill hole were analyzed by XRD using the PVP-10 intercalation method and the computer program MudMaster (Bertaut-Warren-Averbach technique). Mean crystallite thicknesses, as determined from 001 reflections, range from 5–7 nanometers (nm) at depths from 0–1700 ft, then sharply increase to 10–16 nm at depths between 1800–2100 ft, and decrease again to 4–5 nm below this level. The interval of largest particle thickness correlates strongly with the zone of most intense quartz-sericite-pyrite alteration (QSP) and attendant high-density stockwork fracturing, and with the highest concentrations of Mo within the drill core. CTD shapes for the illite particles fall into two main categories: asymptotic and lognormal. The shapes of the CTDs are dependent on conditions of illite formation. The asymptotic CTDs correspond to a nucleation and growth mechanism, whereas surface-controlled growth was the dominant mechanism for the lognormal CTDs. Lognormal CTDs coincide with major through-going fractures or stockwork zones, whereas asymptotic CTDs are present in wallrock distal to these intense fracture zones.

The increase in illite particle size and the associated zone of intense QSP alteration and stockwork veining was related by proximity to the dacitic magma(s), which supplied both reactants and heat to the hydrothermal system. However, no changes in illite polytype, which in other studies reflect temperature transitions, were observed within this interval.

INTRODUCTION

Patterns of hydrothermal alteration, including the presence of classic quartz-sericite-pyrite (QSP) assemblages at Red Mountain, San Juan Mountains, Colorado (Fig. 1), are analogous to similar mineral assemblage zonations found in porphyry Mo and Cu deposits (Munoz 1984; Cox and Singer 1986; Bove and Hon 1992). These similarities include the spatial association of high concentrations of Mo with potassic and superimposed QSP alteration, multiple intrusions, and a relatively high F content of both sericite and secondary biotite. However, the superimposition of a deeply rooted acid-sulfate hydrothermal system on the porphyry-style alteration at Red Mountain has confounded attempts to detect vertical zonation patterns within the earlier-formed QSP assemblage. Difficulty in determining these patterns was largely due to strong overprinting by kaolinite, and possibly by some sericite, that formed during the acid-sulfate alteration event. In this study we use a variety of analytical techniques combined with a new method to describe crystal growth, to characterize zonations and alteration patterns within the deeper QSP assemblage, and to identify conditions for illite formation associated with the hydrothermal system.

BACKGROUND GEOLOGY

Massive alunitization [roughly 70 million metric tons of alunite, $KAl_3(SO_4)_2(OH)$] and subeconomic Mo mineralization at Red Mountain formed by degassing of S-rich dacitic magmas emplaced along the eastern ring fracture zone (Fig. 1) of the 22.9 Ma Lake City caldera (Bove et. al. 1990, 1999). In this deposit (Fig. 2), alunite alteration changes downward through argillic, QSP, and potassic alteration zones that are mostly within intrusions, lavas, and hydrothermal breccias. Quartz-alunite altered rocks (alunite, quartz, and pyrite, with minor topaz, fluorite, pyrophyllite, and gypsum) also grade outward into intermediate through weakly argillized rocks (kaolinite predominant ± primary feldspars), which in turn change laterally into a propylitic alteration assemblage (chlorite, epidote, illite, calcite, and relatively unaltered feldspar) on the periphery of Red Mountain.

Detailed paragenetic studies (Bove et al. 1990; Bove and Hon 1992) demonstrate that the deep-level potassic alteration

* E-mail: dbove@usgs.gov

assemblage (secondary K-feldspar and biotite), which formed from K-rich, magmatic fluids from one or more dacite intrusions, was the earliest alteration assemblage to form at Red Mountain (Fig. 2). The potassic assemblage was in turn superimposed near its top by sericitic alteration related to the QSP assemblage. Although the intensity of QSP alteration increases with depth from the surface, as indicated by an increasing abundance of sericite, secondary quartz, and the absence of primary feldspars, the details of this zonation commonly are obscured by later argillic overprinting. During the later argillic phase, kaolinite overprinted earlier-formed sericite and pyrite in the upper levels of the deep QSP zone. Argillic alteration was mainly coincident with acid sulfate alteration, which formed the quartz-alunite assemblage. Recent $^{40}Ar/^{39}Ar$ geochronologic studies indicate that all hydrothermal stages associated with the Red Mountain system are analytically indistinguishable (<330 000 year maximum age difference) and formed contemporaneously with the 22.9 Ma Lake City caldera (Bove et al. 1999). Detailed mineralogic, petrologic, and stable isotope studies indicate that alunite at Red Mountain formed from buoyant S-rich magmatic vapor plumes emanating from high-level intrusions (Bove et al. 1990). Alunite (δD = –66 to –85 per mil) formed from magmatic-dominant fluids that were isotopically distinct from the meteoric-dominant fluids that formed illite and kaolinite (δD = –115 to –141 per mil) within the argillic and QSP assemblages (Bove et al. 1990).

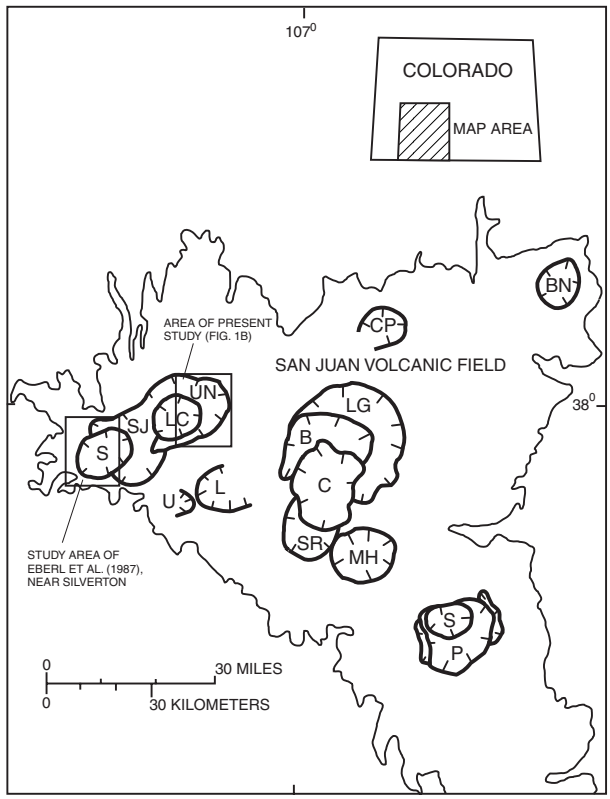

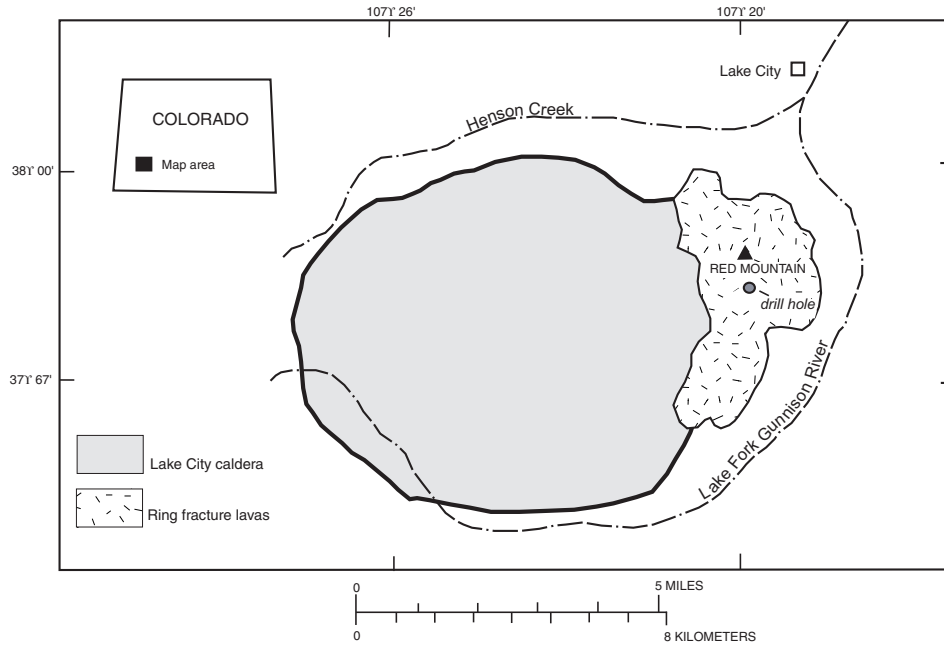

FIGURE 1. (**a**) Map of the San Juan volcanic field, Colorado, showing the general area of the present study. The area of previous study by Eberl et al. (1987), on sericite from the Silverton caldera is also noted. Calderas of the western San Juan Mountains include the Ute Creek (U), Lost Lake (L), Uncompahgre (U), San Juan (SJ), Silverton (S), and Lake City (LC) calderas. Calderas from the central and eastern San Juan Mountains include: La Garita (LG), Bachelor (B), Creede (C), South River (SR), Mount Hope (MH), Cochetopa Park (CP), Silverton? (S), Platoro (P), and Bonanza (B). Modified from Lipman et al. (1997) and Lipman and Steven (1976). (**b**) Map showing location of Red Mountain and deep drill hole.

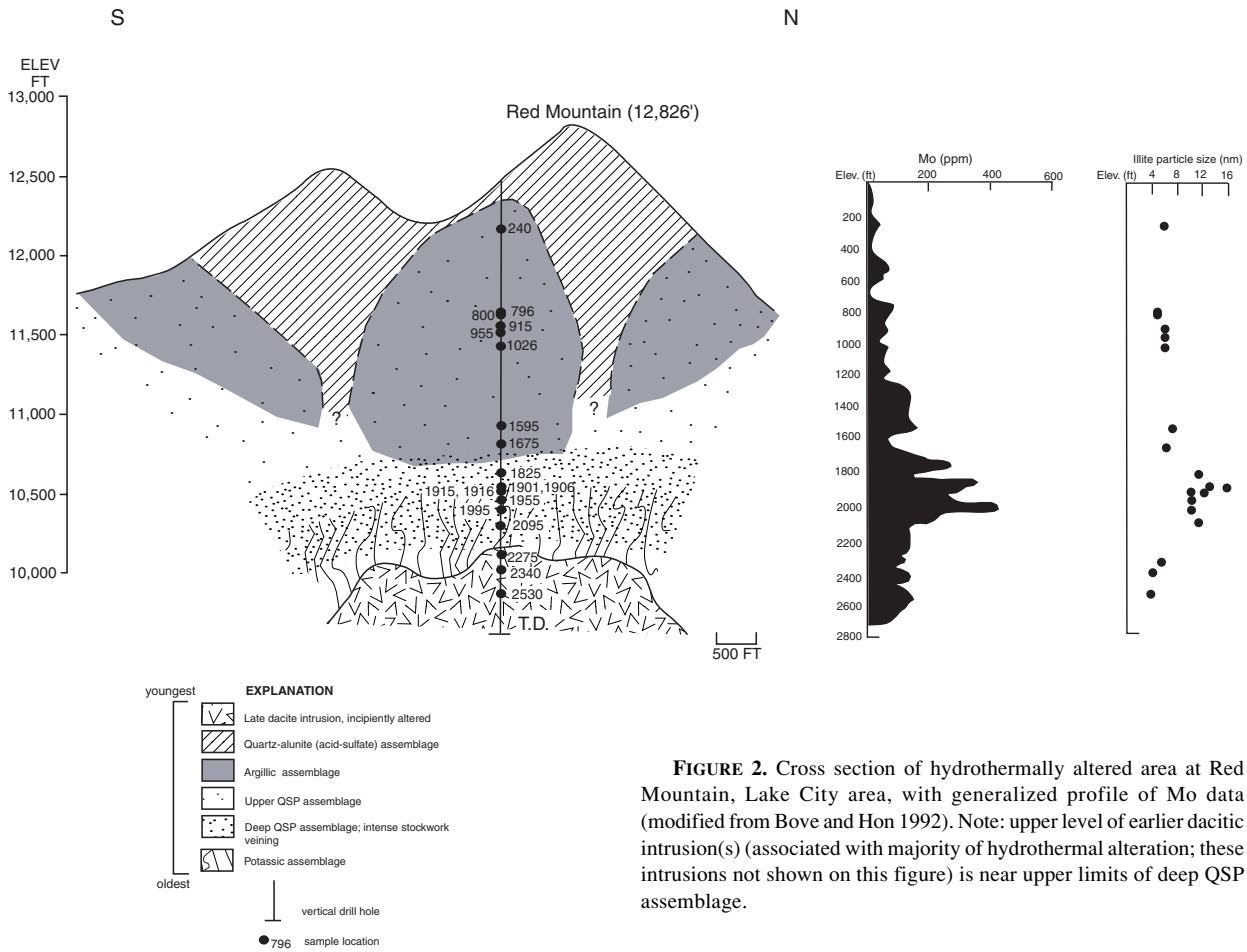

FIGURE 2. Cross section of hydrothermally altered area at Red Mountain, Lake City area, with generalized profile of Mo data (modified from Bove and Hon 1992). Note: upper level of earlier dacitic intrusion(s) (associated with majority of hydrothermal alteration; these intrusions not shown on this figure) is near upper limits of deep QSP assemblage.

EXPERIMENTAL METHODS

Nineteen illites and illite-smectites from a 3000 foot vertical drill hole at the Red Mountain alunite deposit were analyzed by powder X-ray diffraction (XRD) using a Siemens D500 instrument equipped with a Cu tube, a diffracted beam graphite monochromator, and a scintillation detector. The tube current and voltage were 30 mA and 40 kV, respectively. The following slit sizes were used from tube to detector: 1°, 1°, sample, 1°, Söller, monochromator, 0.15°, detector. Scans for expandability measurements were conducted in steps of 0.05° 2θ at 2s per step; those for crystallite size determinations at 0.02° and 5 s and those for random powder preparations at 0.02° and 20 s.

Samples were lightly crushed and disaggregated in distilled water with an ultrasonic probe. The <2-μm (equivalent spherical diameter) size fraction was then separated by aqueous centrifugation and concentrated by ultracentrifugation. Oriented XRD specimens were prepared for measurements of expandability by dispersing approximately 200 mg of Ca-saturated clay (Eberl et al. 1987) in 2 mL of water, pipetting the suspension onto a glass slide, and drying at room temperature. These oriented specimens were analyzed after vapor solvation with ethylene glycol at 60 °C for 12 hr. Polvinylpyrrolidone (PVP-10) intercalated samples were prepared according to Eberl et al. (1998b) and analyzed by XRD after mounting on single-crystal Si wafers. PVP-10 intercalation removes the effects of peak broadening related to swelling so that crystallite thicknesses can be calculated accurately by the Bertaut-Warren-Averbach (BWA) method (Drits et al. 1998). Silicon is used as a substrate to eliminate background intensities from the mount. Randomly oriented samples were prepared by redispersing the clay in 150 mL of distilled water. The suspensions were frozen in a Labconco shell freezer at –30 °C and lyophilized in a Labconco 4.5 freeze drier. The freeze-dried clay was ground lightly with a rubber stopper mounted on a glass rod. Immediately prior to XRD analysis, the freeze-dried samples were heated in an oven at 350 °C for 1 hr. All randomly oriented sample mounts were prepared for XRD by a side-loading method using a sample holder 3 cm long, 2.35 cm wide, and 0.15 cm deep that accommodates approximately 600 mg of clay.

Illite-smectite (I-S) expandability and Reichweite determinations were made from XRD profiles of the oriented clay specimens using the method of Dudek and Środoń (1996), and for some samples by means of the NEWMOD computer program (Reynolds 1985). Illite crystallite thickness was measured by XRD peak broadening of 001 reflections by the BWA method using the computer program MudMaster (Eberl et al. 1996) and PVP-10 intercalation to eliminate the effects of swelling on XRD peak shape (Eberl et al. 1998b). The 005 basal reflections were used with the 001 reflection to determine root mean square of the strain. The Kubler index was determined from illite 001 XRD peak width at half height from oriented air-dried, Na-saturated clay samples. Non-clay mineral identification was based on correspondence between experimental *d*-values with the diagnostic *hkl* reflections from the International Centre for Diffraction Data (1993; ICDD) reference file and/or other published works. Crystal-growth mechanisms and the shapes of crystal-thickness distributions (CTDs) were simulated using the computer program GALOPER (Eberl et al. 2000), which is based on methods for describing both general crystal growth (Eberl et al. 1998a) as well as illite crystal growth (Środoń et al. 2000). Comparison of GALOPER simulated and Mudmaster calculated crystallite thickness distributions were made with the Kolmogorov-Smirnov statistical test (K-S test; Benjamin and Cornell 1970). A significance level >1% determined a match.

The *cis*-vacant (*cv*) and *trans*-vacant (*tv*) layer content and type of rotational disorder in the I-S were determined by modeling each diffraction pattern of the random clay mounts with the computer program WILDFIRE (Reynolds 1993). Initial estimates of *cv* layer content were made using the method of Drits and McCarty (1996). A detailed discussion of the WILDFIRE modeling procedure is found in McCarty and Reynolds (1995).

Major and minor elemental analyses of illites were obtained with a JEOL 8900 electron microprobe at the U.S. Geological Survey, Denver, Colorado. Sample media consisted of polished thin sections and machine conditions were 15 kV accelerating voltage with a 15–20 μm beam width. The analyses were corrected using on-line ZAF correction procedures. Replicate analyses of secondary standards indicated a relative analytical pre*cis*ion of better than ±1 percent (1σ) for major elements. For minor elements, analytical errors are less than the counting statistical standard deviations at the 1σ-level.

Experimental results and discussion

Physical and compositional characteristics of sericite

Sericite[1] at Red Mountain commonly formed as metasomatic replacements after feldspar phenocrysts and groundmass, and as open-space fillings within fractures and in the matrix of hydrothermal breccias (Bove and Hon 1992). Incipient alteration is characterized by a light dusting of sericite after plagioclase phenocrysts and groundmass, accompanied by replacement along microfractures and cleavage planes within sanidine. In contrast, both sanidine and plagioclase may be replaced completely by sericite in intensely altered rocks. Petrographic studies identified multiple generations of sericite, as would be expected in such a complex hydrothermal system with multiple intrusions and overlapping alteration zones (Bove et al. 1990; Bove and Hon 1992).

Observations made with a scanning electron microscope (SEM) reveal individual sericite grains or crystallites massed together to form curved parallel aggregates, although individual crystallites are commonly difficult to differentiate within these masses (Fig. 3a). Sericite aggregates that replace feldspar phenocrysts and fracture-filling crystals consist of individual crystals that range from about 1–3 μm in length and are up to 0.25 μm across, whereas groundmass replacement by sericite is generally finer-grained. SEM studies also detected a morphologically distinct stage of sericite that formed delicate filliform or "flame-tipped" masses (Fig. 3b). Paragenetic studies (Bove et al. 1990) indicate that these fine filliform sericites post-date both the major stages of QSP and argillic alteration (Fig. 2).

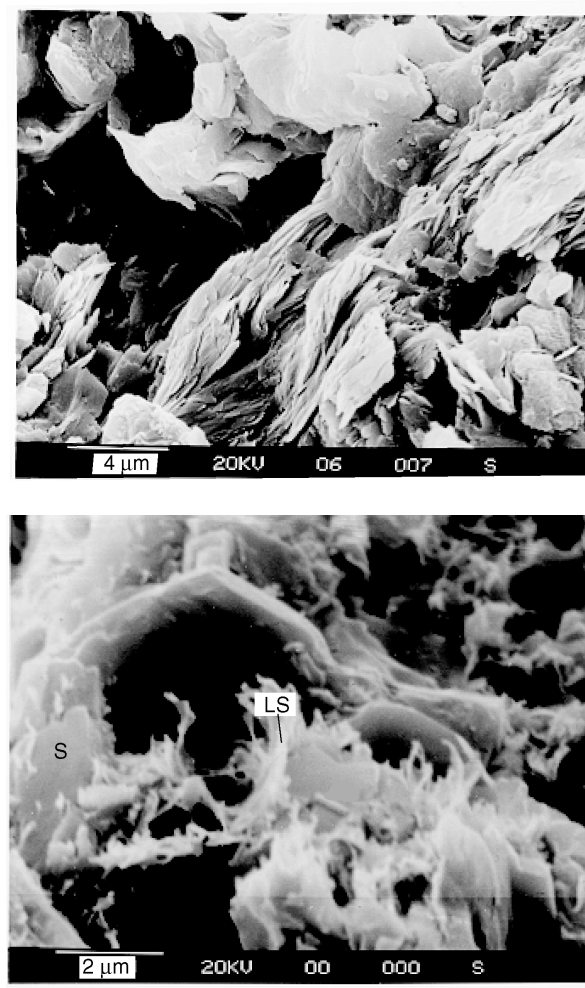

Figure 3. (**a**) SEM photograph of typical sericite as observed in both the upper and lower QSP zones. (**b**) SEM photograph of paragenetically late sericite (LS) with delicate filliform or dendritic morphology growing from substrate of coarser sericite as seen in (**a**).

[1]A petrographic term for fine-grained, highly birefringent micas; term herein used synonymously with illite.

XRD and electron microprobe data (Table 1) demonstrate that sericites at Red Mountain are stacks of thin, Mg-rich, illite crystals with compositions similar to phengite as defined by Środoń and Eberl (1984). Structural formulae, calculated by assuming a negative layer charge of 22 [normalized to $O_{10}(OH)_2$], show interlayer charges ranging from 0.73 to 0.79 equivalents per $O_{10}(OH)_2$. Fluorine content as determined by electron microprobe analysis is appreciable, ranging from 0.5 to 3 wt%; Cl in general was not detected. Using these halogen data, studies by Bove et al. (1990) determined that Red Mountain illites and biotites plot intermediate between micas from typical Cu porphyry systems (low F) and Climax-type, Mo-porphyry systems (high F). Absorption bands diagnostic of NH_4^+ were absent in all five pure-clay separates (<2 μm fraction) analyzed by infrared transmission spectroscopy. Compositional heterogeneity within samples, as shown in Table 1, largely reflects analysis of different stages of illite as determined by cross-cutting and overgrowth relationships. Analysis of these stages by electron microprobe provides evidence of the complex compositions within individual hydrothermal illite samples.

TABLE 1. Chemical compositions of Red Mountain illites determined by electron microprobe analyses

Sample	1916-5 pt4	1916-5 pt3	1906-2 pt5	1906-2 pt3	1906-3 pt6	1955-1 pt9
SiO_2	53.26	53.75	50.50	51.26	51.81	54.45
Al_2O_3	24.42	24.97	27.77	31.57	30.92	26.30
FeO	0.30	0.26	0.23	0.28	0.48	0.33
MnO	0.01	0.01	0.02	0.00	0.03	0.01
MgO	3.81	3.94	2.52	1.87	1.95	3.60
CaO	0.01	0.01	0.00	0.03	0.00	0.00
BaO	0.04	0.00	0.03	0.03	0.06	
Na_2O	0.08	0.13	0.10	0.08	0.17	0.05
K_2O	8.56	8.68	8.52	9.22	9.25	8.56
F	2.63	2.66	1.89	1.57	1.45	2.40
Cl	0.03	0.01	0.05	0.03	0.02	0.02
Total	93.15	94.42	91.63	95.94	96.14	95.72
Tetrahedral						
Si	3.63	3.61	3.48	3.36	3.4	3.59
Al	0.37	0.39	0.53	0.64	0.61	0.41
Octahedral						
Al	1.6	1.59	1.73	1.8	1.78	1.63
Fe	0.02	0.02	0.01	0.02	0.03	0.02
Mn	0	0	0	0	0	0
Mg	0.39	0.4	0.26	0.18	0.19	0.35
Interlayer						
Ca	0	0	0	0	0	0
Ba	0	0	0	0	0	0
Na	0.01	0.02	0.01	0.01	0.02	0.01
K	0.75	0.74	0.75	0.77	0.77	0.72
F	0.57	0.57	0.41	0.33	0.3	0.5
Cl	0	0	0.01	0	0	0
OH	1.43	1.43	1.58	1.67	1.7	1.5

Sample	1955-1 pt9	1955-1 pt6	1414-1 pt1	1414-2 pt2	1414-3 pt2
SiO_2	54.45	53.54	48.04	50.05	48.59
Al_2O_3	26.30	24.66	27.81	27.84	27.11
FeO	0.33	0.11	0.53	0.56	0.49
MnO	0.01	0.02	0.02	0.01	0.01
MgO	3.60	3.98	1.79	1.76	2.00
CaO	0.00	0.00	0.01	0.00	0.00
BaO					
Na_2O	0.05	0.00	0.13	0.03	0.10
K_2O	8.56	8.63	7.76	8.26	8.15
F	2.40	2.34	1.31	0.53	0.94
Cl	0.02	0.01	0.24	0.23	0.14
Total	95.72	93.29	87.64	89.27	87.53
Tetrahedral					
Si	3.59	3.62	3.43	3.49	3.47
Al	0.41	0.38	0.57	0.51	0.53
Octahedral					
Al	1.63	1.59	1.78	1.78	1.76
Fe	0.02	0.01	0.03	0.03	0.03
Mn	0	0	0	0	0
Mg	0.35	0.4	0.19	0.18	0.21
Interlayer					
Ca	0	0	0	0	0
Ba					
Na	0.01	0	0.02	0	0.01
K	0.72	0.75	0.71	0.74	0.74
F	0.5	0.5	0.3	0.12	0.21
Cl	0	0	0.03	0.03	0.02
OH	1.5	1.5	1.68	1.86	1.77

Notes: First four numbers of "sample" represent actual sample number. Total Fe as FeO. TiO_2 and H_2O not analyzed. Structural formulae calculated by normalizing analyses to a theoretical structure containing $O_{10}(OH)_2$.

Changes in illite particle thickness with depth

Illite formed during a major episode of quartz-sericite-pyrite alteration, the intensity of which varies systematically with depth throughout the entire drill core. Changes in mean illite particle thickness with depth, measured by the BWA method from PVP-10 intercalated samples, are summarized in Table 2, column 4, and in Figures 2 and 4.

Mean thickness ranges from 5–7 nanometers (nm) at depths from 240–1700 ft, sharply increases to 10–16 nm at depths of 1800–2100 ft, and decreases again to 4–5 nm at depth below 2100 ft (Fig. 4). The interval of greatest illite particle thickness correlates strongly with the zone of most intense QSP alteration and attendant high-density stockwork veining, and with the consistently highest values of Mo within the drill hole (Fig. 2). Concentrations of Mo, which is present as molybdenite mainly along hairline fractures, are greatest from about 1700 to 2150 ft, ranging from 150 to 450 ppm in eleven samples from within this zone (Bove and Hon 1992). Molybdenum concentrations generally are less than 100 ppm above 1700 ft and less than 200 ppm below 2150 ft. Furthermore, this same interval correlates with the uppermost level (~1800 ft) of one or more dacite porphyry intrusions (relationship established in drill core studies; Bove and Hon 1992; these intrusion(s) not portrayed on Fig. 2), which were the source of heat and fluids that sustained the zoned hydrothermal system (Bove et al. 1990).

The level of most intense alteration also is defined in a plot of the Kubler illite crystallinity index (Kubler 1968; Warr and Rice 1994) with depth, although the zone is not defined as clearly as in the plot of illite thicknesses (Fig. 4). Swelling and CTD shape, as well as crystallite size, influence measurement of the Kubler index (Drits et al. 1997). BWA calculations using the Mudmaster program involve no assumptions with respect to the shape of the XRD peak (the raw XRD data is used) or with respect to the shape of the crystallite thickness distribution (which is determined in the method), and swelling is removed by PVP-10 intercalation.

Although mean illite particle size is similar above and be-

TABLE 2. Changes in illite parameters with depth for the hydrothermal system

Depth (ft)	Fracture or wall-rock	Exp. (%)	Thick. (nm)	Root mean Sq. strain (Å)	α	β^2	CTD shape	Nuc. + growth	Surface-controlled	Add. Nuc.	K-S test (%)
240	W	n.d.	5.7	0.16	1.40	0.58	Asymp.	n.d.	n.d.	n.d.	n.d.
796	F	(14)	5	0.26	1.50	0.24	Lognor.	3	1	0	1 to 5
800	W	(25)	5.3	0.21	1.42	0.47	Asymp.	5	0	0	5 to 10
915	W	(15)	6.3	0.21	1.62	0.41	Asymp.	4	0	100	>10
955	F	(17)	6.1	0.18	1.60	0.39	Lognor.	4	0	125	>10
1026	W	(17)	5.9	0.0	1.48	0.47	Asymp.	5	0	0	5 to 10
1595	W	4	6.6	0.05	1.59	0.54	Asymp.	6	0	25	>10
1675	W	5	6.2	0.16	1.58	0.47	Asymp.	6	0	25	1 to 5
1825	F, FZ	2	11.1	0.20	2.24	0.32	Lognor.	3	3	0	5 to 10
1901	FZ	4	12.9	0.14	2.37	0.37	Lognor.	4	3	0	5 to 10
1906	F, FZ	n.d.	16.1	p.i.	2.61	0.37	Lognor.	3	4	0	>10
1915	FZ	n.d.	10	0.32	2.09	0.45	Lognor.	5	2	0	>10
1916	F, FZ	2	12.3	0.16	2.26	0.49	Lognor.	4	2	0	1 to 5
1955	FZ	2	9.5	0.15	2.04	0.48	Lognor.	5	2	0	1 to 5
1995	FZ	n.d.	10.3	0.0	1.76	1.06	Asymp.	8	0	175	1 to 5
2095	FZ	n.d.	11.5	.11	2.18	0.51	Lognor.	5	2	0	>10
2275	W	n.d.	5.3	n.d.	1.35	0.50	Asymp.	5	0	175	5 to 10
2340	W	n.d.	3.7	p.i.	1.16	0.27	Asymp.	4	0	150	1 to 5
2530	W	n.d.	4.3	n.d.	1.25	0.35	Asymp.	4	0	150	>10

Notes: Expandabilities in parentheses are for I-S mixed with less expandable component. K-S test = level significance of the Kolmogorov-Smirnov statistical test in comparing Galoper simulated with MudMaster measured illite thickness distributions; n.d. = not determined; p.i. = peak interference. F = fracture sample; W = wallrock sample; FZ = zone of high density fracturing.

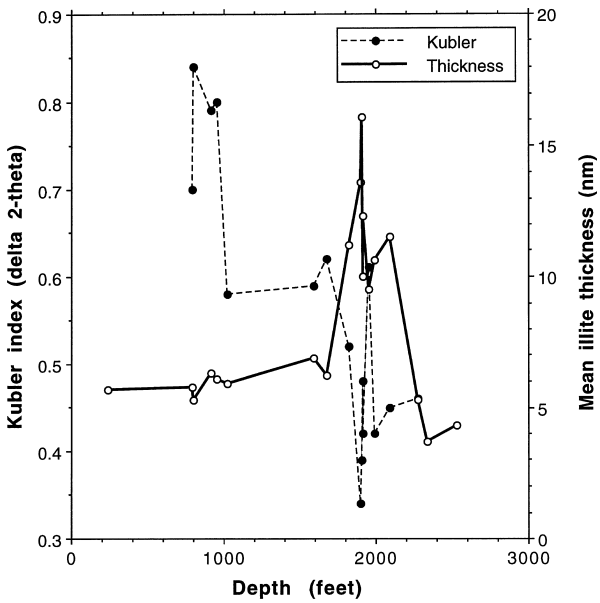

FIGURE 4. Change in mean illite crystallite thickness with depth and Kubler illite crystallinity index with depth. Note: increasing crystallinity from Kubler index corresponds with lower values on the Y-axis.

low the 1800–2100 ft interval, the conditions under which the respective illites formed were quite different. As shown in Figure 2, illite formed within the upper 2200 feet of core is largely associated with QSP alteration zones, upon which were superimposed a later argillic alteration event; primary igneous mineral phases are rarely preserved within these alteration zones. In contrast, illite within the lower section of core (>2200 ft) reflects weak alteration within intrusions that post-date the main stages of hydrothermal alteration (Bove and Hon 1992). Primary igneous mineral phases within this interval of core generally have not been altered.

Illite particle thickness from higher-order 00*l* reflections also were calculated to test for quality of sample preparation (by comparison to 001 calculations; Eberl et al. 1998b) and to determine strain broadening. In many samples, peak interference due to subordinate phases (Table 2) prevented accurate thickness calculations for the 002 and 003 reflections; however, 005 reflections generally produced good results. Root mean squares of the strain varied from zero to 0.32 Å (Table 2), which are similar to those measured on a variety of illites by Eberl et al. (1998b), and strain generally had a Gaussian distribution.

Shapes of illite crystallite thickness distributions

Illite crystallite thickness distributions in these samples have two general shapes (Table 2 and Fig. 5): asymptotic (Fig. 5a), and lognormal-like (Fig. 5b). Generally, illites sampled at depths from zero to 1675 ft had asymptotic shapes, but two samples were found to be lognormal. Samples with asymptotic CTDs in the 0–1675 ft interval were collected in zones devoid of significant clay-lined or mineralized fractures or dense fracture zones, whereas the lognormal shapes correspond to illites formed within prominent brecciated fracture zones. Samples from the interval 1825 to 2095 ft generally are lognormal. Several of the lognormal samples had a spike in the CTD at 2 nm, which is thought to be an artifact of the calculation, and was removed by smoothing. The bimodal samples are characterized by a lognormal-shaped CTD with an additional mode at 2 nm. This entire core interval is associated with high-density stockwork fracturing and intense QSP alteration. Asymptotic CTDs in the lower 400 ft of drill core correspond to illite located distal to zones of strong fracturing. Thus, lognormal shapes are mostly coincident with strong fracturing, whereas asymptotic CTDs represent wallrock distal to intense fracture zones.

The CTDs can be characterized further by α and β^2, where α is the mean of the natural logarithms of the thicknesses, defined as $\alpha = \Sigma \ln(t) f(t)$, where $f(t)$ is the frequency of thickness t and β^2 is the variance of the natural logarithms of the thicknesses, defined as $\beta^2 = \Sigma(t - \alpha)^2 f(t)$ (Eberl et al. 1998a). These parameters are plotted for the two thickness distribution shapes

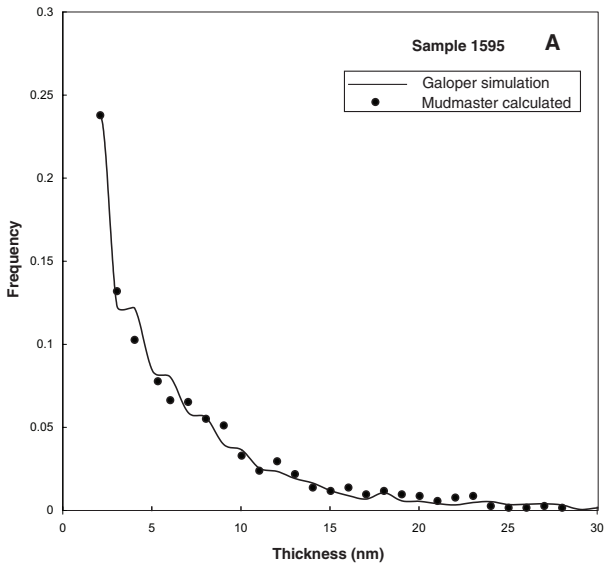

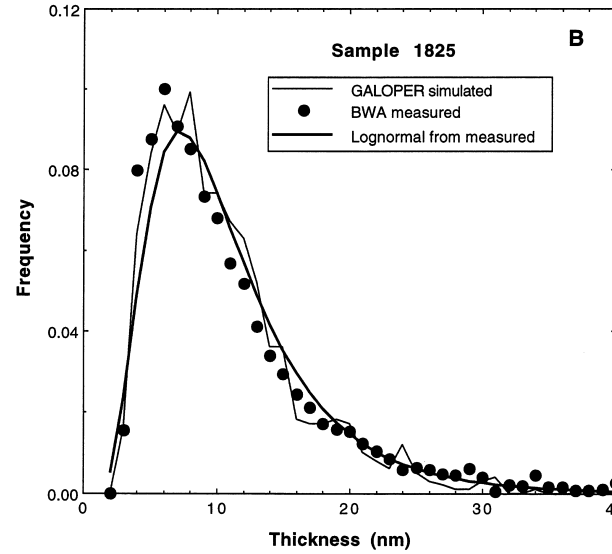

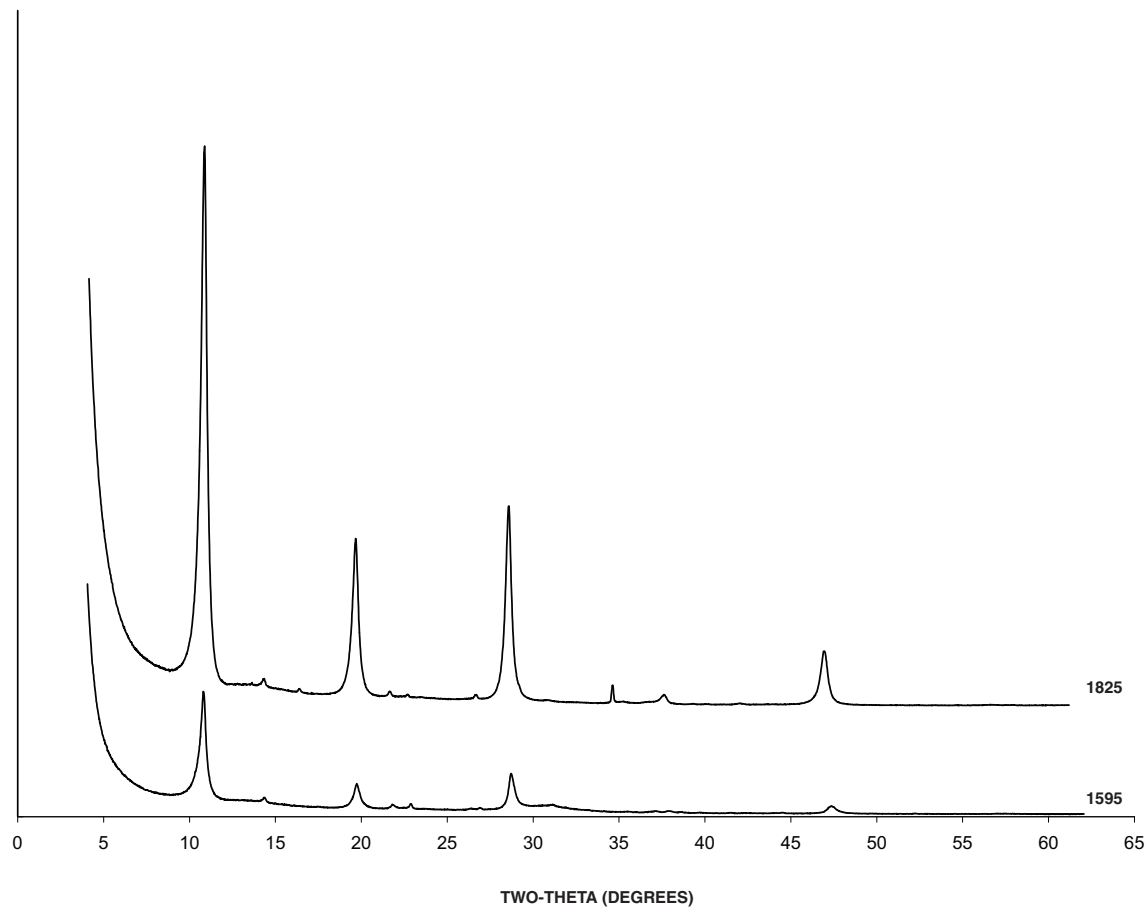

FIGURE 5. (**a**) Asymptotic and (**b**) lognormal-like shapes for illite crystallite thickness distributions found in the Red Mountain clays. (**c**) XRD patterns for samples portrayed in figures (**a**) and (**b**). Samples Na-saturated, treated with PVP-10, and mounted on Si-wafers.

in Figure 6, together with theoretical paths for two crystal-growth mechanisms: (1) constant-rate nucleation accompanied by surface-controlled growth (curve A-B), and (2) surface-controlled growth (curves that trend somewhat parallel to A-C) without simultaneous nucleation (Eberl et al. 1998a).

With the aid of the $\alpha - \beta^2$ diagram (Fig. 6) and the GALOPER computer program, reaction pathways for crystal growth of Red Mountain illite can be simulated. The asymptotic distributions plot near the path expected for constant-rate nucleation and growth (path A-B, Fig. 6). Crystal growth according to this mechanism proceeds first with the constant rate nucleation of 2 nm-thick illite, which subsequently experience size-dependent growth by the Law of Proportionate Effect (LPE; Eberl et al. 1998a; Środoń et al. 2000); inherently, β^2 increases exponentially with α, and the distributions are expected to have asymptotic shapes. Path A-C in Figure 6 is that expected if all of the crystals nucleate at the same time, and then undergo LPE surface-controlled growth, giving rise to lognormally shaped distributions. Crystal distribution shapes also may follow path A-B for a time as they experience simultaneous nucleation and growth, and then follow one of the paths above and parallel to path A-C as nucleation ceases and the crystals continue to grow. During this process, asymptotic distributions of crystals created along path A-B are transformed into lognormal-like distributions as they subsequently follow one of the paths parallel to A-C.

The numbers that mark the intersections of path A-B (Fig. 6) with the paths near-parallel to A-C indicate the number of nucleation and growth simulation cycles used in the Galoper program to reach the α and β^2 of the intersection by the nucleation and growth mechanism. For example, because the program can nucleate 1001 potential crystals, the intersection marked "2" indicates that 500 two-nm-thick crystals nucleated during the first calculation cycle, followed by a second cycle during which 500 more crystals nucleated and the first 500 crystals grew one cycle by the LPE. The "3" indicates a longer lasting nucleation and growth mechanism, during which 333 crystals nucleated per cycle and grew similarly. Tick marks on the paths parallel to A-C (Fig. 6) indicate the number of calculation cycles for growth only. From the location of sample α and β^2 parameters on this diagram, and through trial and error using the GALOPER program, one can simulate reaction pathways for the illites.

For example, the lognormal crystallite thickness distribution of sample 1901 (Fig. 6 and Fig. 7) can be simulated as follows. First, the illite underwent simultaneous nucleation and growth, following path A-D (Fig. 7) for 4 calculation cycles, during which 250 crystals nucleated per cycle in the GALOPER program. This mechanism gives rise to an asymptotic thickness distribution (Fig. 8a). Nucleation and growth was followed by growth only (Fig. 7, path D-E) during which the asymptotic distribution was transformed into a lognormal distribution (Fig. 8b). Using this reasoning, distribution shapes for the samples were simulated using one or two growth mechanisms, a number of calculation cycles, and sometimes additional nuclei for the asymptotic CTDs. The results are listed in columns 9 through 11 of Table 2. A simulation was determined successful if the level of significance in the K-S test for comparison with the measured distribution was >1% (last column in Table 2). Lack of a match between simulated and measured distributions for other reaction pathways for sample 1901 through the $\alpha - \beta^2$ diagram indicates that there may be a limited number of paths through the diagram by which the shape of the thickness distribution can be simulated. For example, if one simulates 5 (rather than 4) nucleation and growth cycles for sample 1901, followed by two growth cycles, the simulated CTD has approximately the same mean and variance as the previous simulation, but the simulated and the measured distribution cannot be matched by

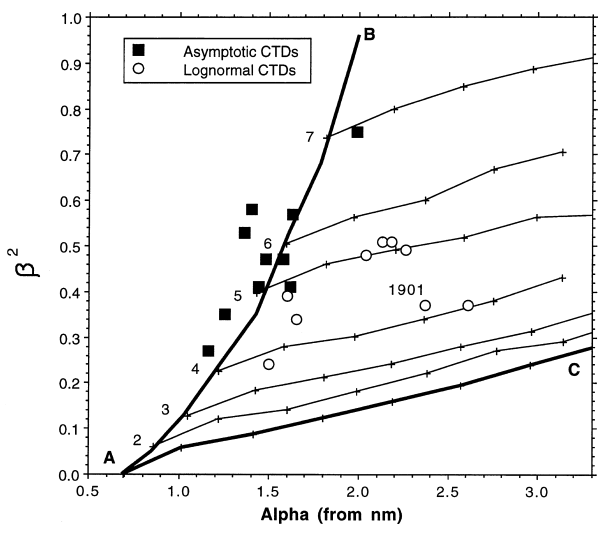

FIGURE 6. Alpha-β^2 diagram showing these parameters for illite crystallite thickness distributions having the two basic shapes. See text for explanation.

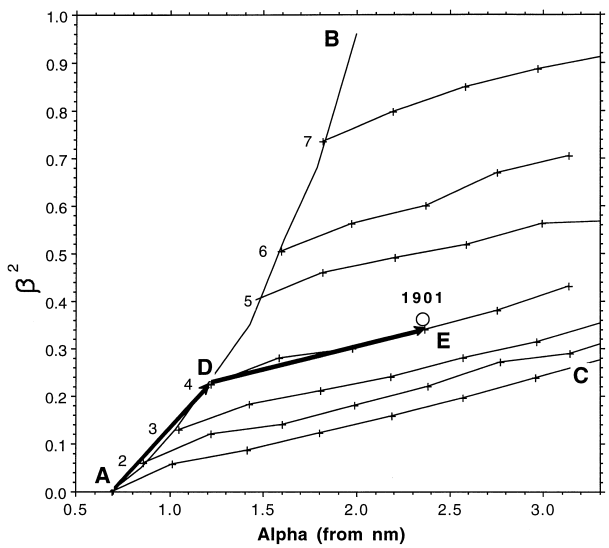

FIGURE 7. Alpha-β^2 digram showing the unique reaction path (A-D-E) that simulates the shape of the crystallite thickness distribution for sample 1901.

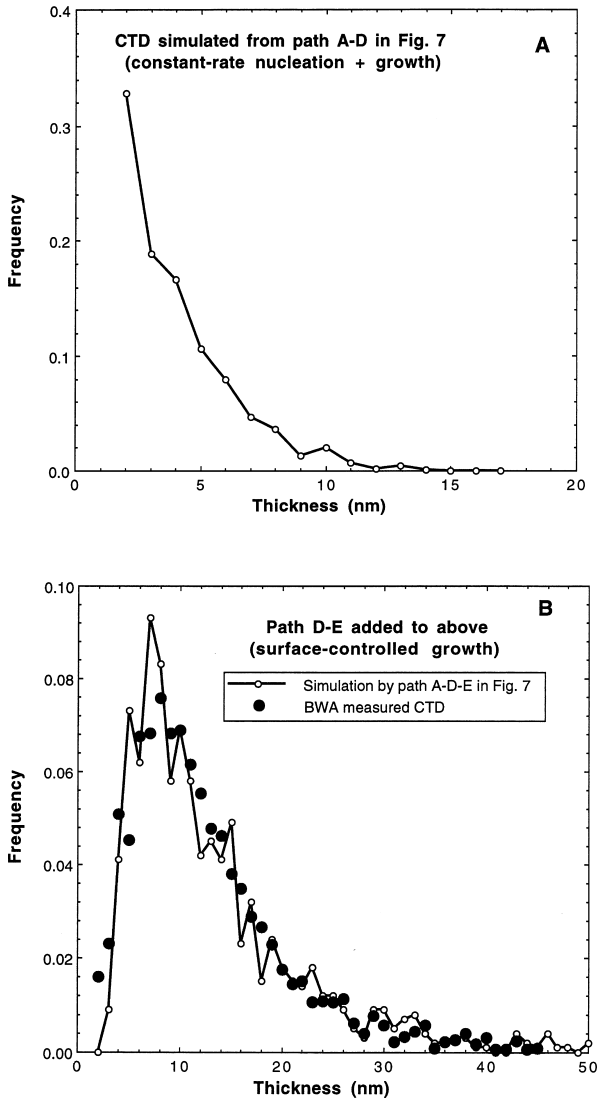

FIGURE 8. (**a**–**b**) How the shape of the crystallite thickness distribution for sample 1901 changes as the reaction progresses along the path given in Figure 7.

statistical testing. Therefore, the shapes of the CTDs depend on the reaction path.

Expandability

The presence of two overlapping peaks in the 17–18 °2θ range on XRD profiles in several samples from the upper section of drill core (samples 796, 915, 955, and 1026) prevented accurate expandability measurements by conventional interpretive methods. The expandability of both I-S phases in these samples was determined by decomposing the composite peak between 17–18 °2θ into its illite and I-S components using the Siemens D5000 FIT software program with a split Pearson function and separate exponents.

As shown in Table 2, all five illites sampled from the upper 1000 ft of drill core contain an I-S component with relatively high expandablity (14–25%) and ordering of R ≤ 2. With the exception of sample 800 (Table 2), these five samples also contain an illite phase with expandabilities ranging from 2–6%. Illites from the deeper section of drill core lack an expandable I-S component, have R ≥ 3, and have expandabilities (2–4%) in the same range as those found for near end-member illite within the upper section of the core. It is possible that expandable I-S found at shallow depths was formed by leaching of K from illite interlayers during either the acid-sulfate hydrothermal event or by low pH meteoric waters derived by oxidation of high volumes of finely disseminated pyrite (Bove et al. 1990). The leaching of interlayer K is supported by the anomalously low K content within illites in the upper levels of drill core as determined by electron microbe analysis (Bove 1988). Therefore, the presence of the more expandable phase within these shallow interval samples would define the reach of the acid-sulfate alteration or the depths to which low pH meteoric waters circulated.

Illite-smectite three-dimensional structure

Three-dimensional crystal structures of I-S were modeled with WILDFIRE using combinations of the program input parameters P_{cv}, P_0, and P_{60} (Table 3; Figs. 9a and 9b). P_{cv} refers to the content of *cis*-vacant (*cv*) layers interstratified with *trans*-vacant (*tv*) layers in the crystallite, where:

$$P_{cv} + P_{tv} = 1.0.$$

P_0 is the percentage of layers rotated zero degrees with respect to a preceding adjacent layer. $P_0 = 1.0$ describes the 1*M* polytype where all layers have the same orientation. Rotations of n·60° were not detected in the samples modeled in this study. The data (Table 3) indicate that there is little systematic change in three-dimensional structure with depth, except that the shallowest two samples (796 and 1564) have a smaller percentage of P_0 rotations. It is noteworthy that these two samples have thinner corresponding particle size (<6 nm) than the remaining samples with higher percentage of P_0 rotations (>11 nm). However, a larger sample set showing this correlation is needed to characterize this association definitively. The physical and chemical conditions resulting in these various 1*M* structural modifications and their octahedral cation distributions are not known at this time (cf. Drits et al. 1993; McCarty and Reynolds 1995; Drits et al. 1996).

Reflectance spectroscopy and particle size

Reflectance spectra (0.1 to 6.0 micrometer range) for eight <2 μm illite separates of varying particle size were measured using a Nicolet 760 Fourier transform spectrometer. Measurements were made on packed powders in a CO_2- and H_2O-purged atmosphere. The purpose of this study was to determine whether differences in particle size could be detected by remotely sensed spectroscopy. After background removal, values of band depth and width, and various depth ratios for key illite absorption features (1.41, 2.2, 2.34, and 2.44 μm) were compared among samples. Various plots of these data, however, failed to reveal any systematic relationship between particle size or CTD shape and any of the above absorption bands. Similar results were

TABLE 3. Input parameters for WILDFIRE modeling of three-dimensional I-S structures

Depth (ft)	P_0	P_{cv}	P_{60}	Other minerals present
796	0.75	0.20	0	quartz, jarosite (?), alunite, anatase, svanbergite
1564	0.70	0.20	0	quartz, gypsum (?), alunite, anatase, svanbergite
1825	0.90	0	0	svanbergite (?)
1901	0.80	0.20	0	quartz, gypsum (?), alunite, anatase, svanbergite
1906	0.90	0.25	0	phillipsite (?), alunite, svanbergite
1916	0.90	0.10	0	quartz, halite
1955	0.95	0.30	0	quartz, kaolinite, alunite

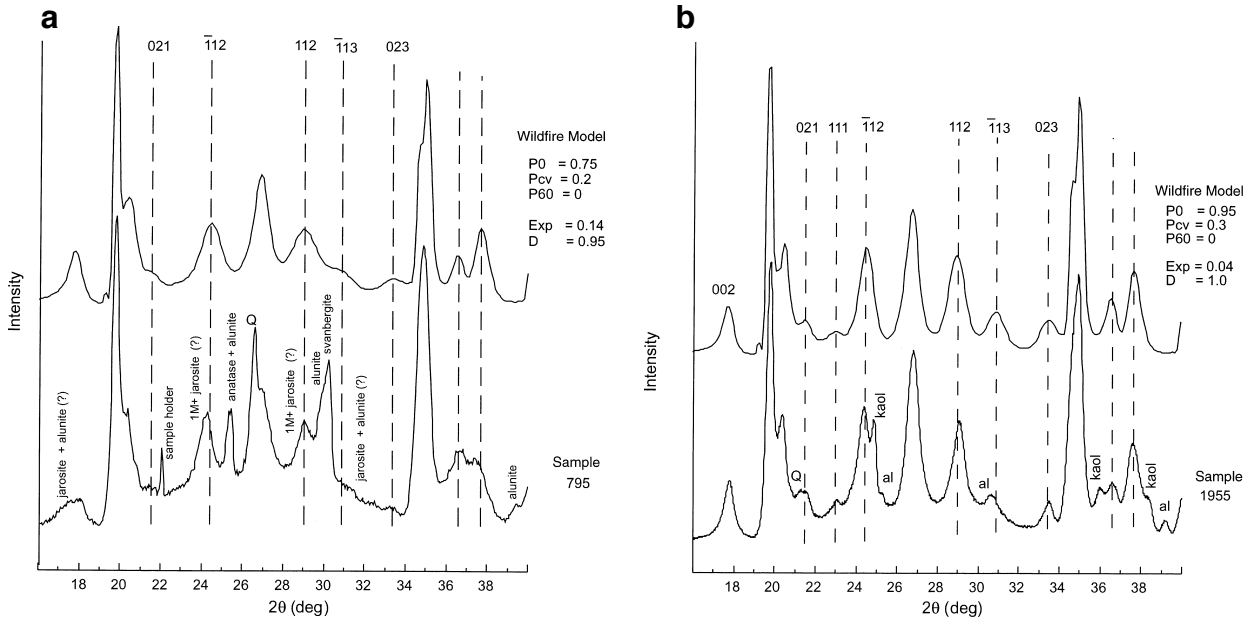

FIGURE 9. (**a** and **b**) Comparison between calculated (left) and experimental diffraction patterns for two representative samples modeled by WILDFIRE. The parameters are: $P_0 = 0.75$, $P_{cv} = 0.2$, $P_{60} = 0$, expandability = 0.14, D = 0.95. Other minerals and the *hkl* indices for the calculated pattern are shown on the figure, Q = quartz.

also observed in hydrothermal illite from Silverton, Colorado, about 40 km west of Lake City (D. Bove, USGS, unpublished data, 2000).

DISCUSSION

Illitic clays increase in thickness in the zone of most intense QSP alteration, a depth that corresponds to (1) the emplacement of one or more dacite intrusions, (2) the presence of stockwork veining and fracturing, and (3) elevated concentrations of Mo (Fig. 2 and 3a). The formation of thicker particles within this zone may relate to close proximity to the dacitic magma(s), which supplied both reactants and heat to the hydrothermal system. Fractures provided pathways for reactants, but the association of thin particles with a fracture-related illite in the upper drill core (Table 2; Fig. 2) indicates that fracture conduits alone—without the combined effects of both elevated temperature and reactant supply (due to near proximity to a magmatic source)—were insufficient to promote the growth of thicker crystals.

Only the 1*M* polytype was identified throughout the entire drill core. In other similar hydrothermal systems throughout the San Juan Mountains, transitions from the 1*M* to $2M_1$ polytype, similar to those observed in metamorphic systems (Środoń and Eberl 1984), correlate with both temperature variation and distance from centers of hydrothermal alteration (Eberl et al. 1987; Bove et al 1996; Bove, unpublished data, 2001). Such contrasts are especially noted in the Red Mountains acid-sulfate system, near Silverton, Colorado (Fig. 1), which is similar in age and genesis to Red Mountain at Lake City (Eberl and others 1987; Bove and others 2000). Sericites within QSP zones associated with the acid-sulfate assemblage near Silverton (Red Mountains area) are dominantly mixtures of the $2M_1$ and 1*M* polytypes, although several samples contain only the 1*M* polytype (Eberl et al. 1987; Bove, unpublished data, 2001). In addition, these QSP-related sericites are generally thicker than their Lake City counterparts, ranging from 11 to 36 nm, and averaging 17 nm (Bove et al. 2000). However, poorly crystalline sericite that formed within the "weak sericite-pyrite" margins of the Silverton system (1*M* polytype) have particle sizes ranging only from 4 to 8 nm (Bove et al. 2000). Like the sericite at Lake City, such decreases in particle size are correlated with transitions in alteration intensity, although associated changes in polytype are not observed at Red Mountain-Lake City. One of most striking differences between the Lake City and Silverton "Red Mountains"—the overall size of the respective hydrothermal systems—could conceivably have some bearing on the contrasting particle sizes and nature of the polytypes within these hydrothermal systems. The area of acid-sulfate altered

rock near Lake City is 1.9 mi^2, whereas the Red Mountains acid-sulfate system near Silverton system encompasses nearly 9 mi^2. Compared to Lake City, the much larger Silverton acid-sulfate system may have generated and sustained a more significant heat flux during its evolutionary cycle. If so, this may explain the thicker illite particles and the presence of the $2M_1$ polytypes within the generally hotter Silverton hydrothermal system.

The two shapes for illite thickness distributions, asymptotic and lognormal, with the latter being found most commonly in fractured and intensely QSP-altered rock, correspond to two crystal-growth mechanisms. Modeling using the GALOPER program suggests that illites with asymptotic CTDs evolved by a mechanism of constant-rate nucleation and growth. These crystals likely formed in highly supersaturated solutions that could sustain nucleation. These conditions are consistent with mineral reactions in wallrock (distal to fractures) where alteration involved the destruction of primary feldspars and devitrified groundmass, with the subsequent release of high concentrations of cations to the surrounding fluids. In contrast, GALOPER simulations indicate that illites with lognormal CTDs grew initially by nucleation and growth that was followed by surface-controlled growth as the level of supersaturation decreased. Levels of supersaturation within the fracture zones would likely be less than in the wallrock, because fractures would have greater water/rock ratios. Continued supply of K-rich fluids to the fractures may have sustained crystal growth longer within the fractures than in the adjacent wallrock, and more material was used by the lognormal CTDs for growth, rather than for both nucleation and growth. Both of these effects may have led to thicker crystals for the lognormal CTDs.

Later overprinting by a shallow, acid-sulfate event or by low pH meteoric waters may have opened illite layers by leaching of interlayer K, giving rise to mixtures of illite and more expandable illite-smectite.

REFERENCES CITED

Benjamin, J.R. and Cornell, C.A. (1970) Probability and decision for civil engineers, 684 p. McGraw-Hill, New York.

Bove, D.J. (1988) Evolution of the Red Mountain alunite deposit, Lake City caldera, San Juan Mountains, Colorado, Unpub. M.A. thesis, University of Colorado, Boulder, 179 p.

Bove, D.J. and Hon, K. (1992) Geologic and alteration map with drill-core logs of the Red Mountain area near Lake City, Hinsdale County, Colorado. U.S. Geological Survey Miscellaneous Investigations Map I-2286.

Bove, D.J., Rye, R.O., and Hon, K. (1990) Evolution of the Red Mountain alunite deposit, Lake City, Colorado. U.S. Geological Survey Open-File Report 90-0235, 30 p.

Bove, D.J., Wilson, A.B., Barry, T.H., Hon, K., Kurtz, J., VanLoenen, R.E., and Calkin, W.S. (1996) Geology, alteration, and rock and water chemistry of the Iron, Alum, and Bitter Creek areas, Upper Alamosa River, southwestern, Colorado. U.S. Geological Survey Open-File Report 96-039, 34 p.

Bove, D.J., Hon, K., Slack, J.F., Budding, K.E., Slack, J.F., and Yeoman, R.A. (1999) Geochronology and geology of late Oligocene through Miocene volcanism and mineralization in the western San Juan Mountains, Colorado. U.S. Geological Survey Open-File Report 99-347, 35 p.

Cox, D.P. and Singer, D.A., Eds. (1986) Mineral deposit models. U.S. Geological Survey Bulletin 1693, 379 p.

Drits, V.A. and McCarty, D.K. (1996) The nature of diffraction effects from illite and illite-smectite consisting of interstratified *trans*-vacant and *cis*-vacant 2:1 layers: A semi quantitative technique for a determination of layer-type content. American Mineralogist 81, 852–863.

Drits, V.A., Weber, F., Ls Salyr, A., and Tsipursky, S.I. (1993) X-ray identification of one-layer illite varieties: Application to the study of illites around uranium deposits of Canada: Clays and Clay Minerals, 41, 389–398.

Drits, V.A., Salyn, A.L., and Sucha, V. (1996) Structural transformations of interstratified illite-smectites from Dolná Ves hydrothermal deposits: Dynamics and mechanisms. Clays and Clay Minerals, 44, 181–190.

Drits, V.A., Środoń, J., and Eberl, D.D. (1997) XRD measurement of mean crystallite thickness of illite and illite/smectite: reappraisal of the Kubler index and the Scherrer equation. Clays and Clay Minerals, 45, 461–475.

Drits, V., Eberl, D.D., and Środoń, J. (1998) XRD measurement of mean thickness, thickness distribution and strain for illite and illite-smectite crystallites by the Bertaut-Warren-Averbach technique. Clays and Clay Minerals, 46, p. 38–50.

Dudek, T. and Środoń, J. (1996) Identification of illite/smectite by X-ray powder diffraction taking into account the lognormal distribution of crystal thickness. Geologica Carpathica Clays, 5, 21–32.

Eberl, D.D., Środoń, J., Lee, M., Nadeau, P.H., and Northrup, H.R. (1987) Sericite from the Silverton caldera, Colorado. Correlation among structure, composition, origin, and particle thickness. American Mineralogist, 72, 914–934.

Eberl, D.D., Drits, V., Środoń, J., and Nüesch, R. (1996) MudMaster: A program for calculating crystallite size distributions and strain from the shapes of X-ray diffraction peaks: U.S. Geological Survey Open-File Report 96-171, 46 p.

Eberl, D.D., Drits, V.A., and Środoń, J. (1998a) Deducing growth mechanisms for minerals from the shapes of crystal size distributions. American Journal of Science, 298, 499–533.

Eberl, D.D., Nüesch, R., Sucha, V., and Tsipursky, S. (1998b) Measurement of fundamental illite particle thickness by X-ray diffraction using PVP-10 intercalation. Clays and Clay Minerals, 46, 89–97.

Eberl, D.D., Drits, V.A., and Środoń, J. (2000) Galoper: a program for simulating the shapes of crystal size distributions from growth mechanisms, with associated programs. U.S. Geological Survey Open-File Report 00-505, 44 p.

Kubler, B. (1968) Évaluation quantitative du métamorphisme par la cristallinité de l'illite. Bull. Centre de Recherches de Pau (Socieze Nationale des Pezedes d'Aquitainer), 2, 385–397.

McCarty, D.K. and Reynolds, R.C. Jr. (1995) Rotationally disordered illite/smectite in Paleozoic K-bentonites. Clays and Clay Minerals, 43, 271–284.

Munoz, J.L. (1984) F-OH and Cl-OH exchange in micas with applications to hydrothermal ore deposits. In S.W. Bailey, Ed., Micas, p. 461–491. Reviews in Mineralogy, Mineralogical Society of America, Washington, D.C.

Reynolds, R.C. (1985) NEWMOD computer program for the calculation of the one-dimensional X-ray diffraction patterns of mixed-layer clays. R.C. Reynolds, Dept. of Earth Sciences, Dartmouth College, Hanover, NH 03755.

———(1992) X-ray diffraction studies of illite/smectite from rocks, <1 μm randomly oriented powders, and <1 μm oriented powder aggregates: The absence of laboratory-induced artifacts. Clays and Clay Minerals, 40, 387–396.

———(1993) Three-dimensional powder X-ray diffraction from disordered illite: Simulation and interpretation of the diffraction patterns. In R.C. Reynolds, Jr. and J.R. Walker, Eds., CMS Workshop Lectures, vol. 5, p. 43–77. Computer Applications to X-ray Powder Diffraction Analysis of Clay Minerals, The Clay Minerals Society, Boulder, CO.

Środoń, J. and Eberl, D.D. (1984) Illite. In S.W. Bailey, Ed., Micas, 13, 495–544. Reviews in Mineralogy, Mineralogical Society of America, Washington, D.C.

Środoń, J., Eberl, D.D., and Drits, V.A. (2000) Evolution of fundamental particle size during illitization of smectite and implications for the illitization mechanism. Clays and Clay Minerals, 48, 446–458.

Warr, L.N. and Rice, H.N. (1994) Interlaboratory standardization and calibration of clay mineral crystallinity and crystallite size data. Journal of Metamorphic Geology, 12, 141–152.

MANUSCRIPT RECEIVED APRIL 30, 2001
MANUSCRIPT ACCEPTED JUNE 29, 2002
MANUSCRIPT HANDLED BY JAMES ARONSON